Journal of Materials Chemistry A

Accepted Manuscript

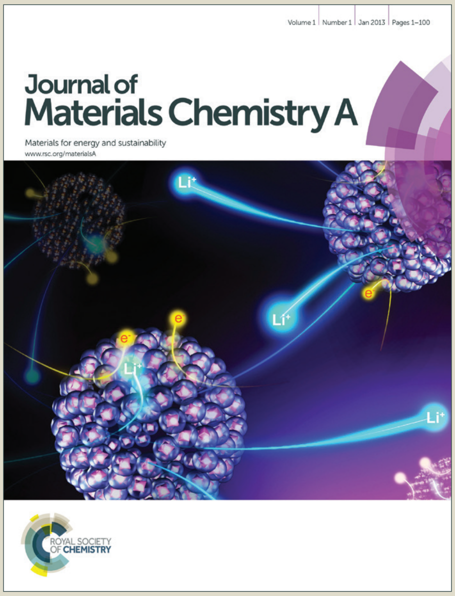

ROYAL SOCIETY
OF CHEMISTRY

www.rsc.org/materialsA

Static and dynamic photoluminescence and photocatalytic properties of uniform, monodispersed up/down-converting, highly luminescent, lanthanide-ion-doped β-$NaYF_4$ phosphor microcrystals with controlled multiform morphologies

Preeti Padhye[†,‡] *and Pankaj Poddar**[†,‡,§]

[‡]*Physical & Materials Chemistry Division, CSIR-National Chemical Laboratory, Pune - 411008, India*

[†]*Academy of Scientific and Innovative Research, Anusandhan Bhawan, Rafi Marg, New Delhi - 110001, India*

[§]*Center of Excellence on Surface Science, CSIR-National Chemical Laboratory, Pune - 411008, India*

Abstract

Lanthanide-ion-doped, single-crystalline hexagonal phase $NaYF_4$ microcrystals with multiform morphologies, such as microrods, hexagonal microprisms, and spindle-like structures were fabricated via cationic/anionic binary capping agents: CTAB and tri-sodium citrate-assisted hydrothermal route. The influence of synthesis conditions on the crystalline morphology was studied and the possible growth mechanisms are presented systematically. The down-conversion and up-conversion photoluminescence (PL) properties of β-$NaYF_4$: Ln^{3+} (Ln=Tb, Yb/Er, and Yb/Tm) were investigated. The static and dynamic PL studies of β-$NaYF_4$:5 % Tb^{3+} showed strong dependence of luminescent properties on the crystalline morphology. Furthermore, the β-$NaYF_4$:5 % Tb^{3+} phosphors exhibited efficient photocatalytic activity under UV as well as solar light irradiation, and showed enhanced selectivity towards methylene blue. Moreover, the morphological effect on the photocatalytic activity of β-$NaYF_4$:5 % Tb^{3+} crystals have also been studied. The high luminescence efficiency and strong photocatalytic activity of β-NaYF$_4$:5 % Tb^{3+}, make them a potential phosphor material and promises to provide a gateway into other applications as in biology and material sciences.

*Corresponding author Email: p.poddar@ncl.res.in

1. Introduction

Due to their unique, tailored, optical properties, lanthanide-ion doped luminescent materials have attracted tremendous attention as phosphors, due to their potential wide-ranging applications as in display devices, solid state lasers, light emitting devices, optical telecommunication, solar cells, fluorescent labels for detection of biomolecules, cell-imaging, catalysis, and medical diagnostics.[1-5] The unique photophysical properties of trivalent lanthanide-ions arise from electronic transitions within the parity forbidden 4*f* shell, which are shielded by filled 5*s* and 5*p* orbitals.[6,7] This unique electronic configuration renders fascinating properties to these materials, such as narrow and sharp emission spectra, long luminescent lifetime, photo-stability, large Stokes and anti-Stokes shift, non-blinking feature, and low autofluorescence. These characteristics of Ln^{3+} doped materials give them an edge over conventional organic fluorescent dyes or quantum-dots for various biological and non-biological applications.[8-11]

To effectively utilize the novel luminescence of Ln^{3+} ions, it is necessary to choose an appropriate host-lattice combination with low phonon-energy to minimize non-radiative losses.[12,13] Among various classes of rare-earth compounds, such as oxides, fluorides, phosphates, vanadates etc., fluorides possess lowest phonon-energy (ca. 350 cm^{-1}) of crystal lattice and wide band gap.[14] Among the investigated rare earth fluorides, $NaYF_4$ possesses low phonon-energy (~ 360 cm^{-1}) and wide band-gap (~ 8 eV).[15] Consequently, $NaYF_4$ is considered to be an excellent and most efficient host matrix for down-conversion (DC) and up-conversion (UC) processes. The crystal structure of $NaYF_4$ exists in two polymorphic forms: cubic (α-) and hexagonal (β-) phases depending upon the crystal growth environment. The cubic phase is a metastable phase and hexagonal phase (β-$NaYF_4$) is thermodynamically stable phase.[16] The hexagonal β-phase $NaYF_4$ is considered a better host than α-$NaYF_4$ for enhanced luminescence efficiency of various optically-active lanthanide-ions.[17,18] The overall luminescence emission of the β-$NaYF_4$ is ~4.4 times greater than those for α-$NaYF_4$.[19] Thus, it is desirable and important to synthesize hexagonal β-$NaYF_4$ phase to achieve a brighter phosphor.

In modern chemistry and materials science, the precise architectural manipulation of anisotropic crystals with well-defined morphologies and accurately tunable sizes remain a research focus and a challenging issue due to the fact that the physical, chemical, luminescent, magnetic and catalytic properties of the materials are closely interrelate with geometrical factors such as shape, size, and crystalline facets.[20,21,22] Moreover, various properties of the materials often significantly vary for different crystalline facets, as demonstrated by our group previously.[23]

In the growth process of crystals, a series of external factors, such as reaction temperature, time, pH of precursor-solution, and organic additives drastically influence the shape-evolution of the crystals. A variety of organic additives and shape directing agents such as sodium citrate[24,25], ethylenediaminetetraacetic acid (EDTA)[26,27], cetyltrimethylammonium bromide (CTAB)[28], oleic-acid[29,18], sodium dodecylbenzenesulfonate (SDBS)[30] etc. are used to control and tune the crystallinity, and morphology of the anisotropic crystals. The capping-agents get selectively adsorbed on certain crystalline facets, inducing anisotropic growth[31] and the difference in the relative growth-rates of various crystal facets results in a diverse outlook of the crystallites.

The mixed cationic/anionic surfactants represent an interesting binary capping agent-directed synthesis system by controlling the nucleation and growth via synergistic interactions of binary surfactant molecules with metals ions, as well as specific crystalline planes.[32] Earlier studies have shown the successful use of such system in the shape control of semiconductors and metal nanocrystals.[33,34] Highly uniform star-shaped and octahedral PbS nanocrystals[33]and single-crystalline gold nanobelts and nanocombs[34] were formed in the presence of the cationic surfactant CTAB and the anionic surfactant sodium dodecyl sulphate (SDS). Rare-earth-ion-doped hexagonal-phase $NaYF_4$ nanowires were hydrothermally synthesized at the cooperative effect of sodium citrate with anionic surfactant sodium bis (2-ethylhexyl) sulfosuccinate (AOT).[35] Nevertheless, the effect of presence of both cationic CTAB and anionic trisodium citrate (TSC) surfactants together, and their optical studies is being rarely explored. Moreover, these materials are expected to show photocatalytic properties, but only few reports of lanthanide-ion doped materials are known till date. Recently, the photocatalytic activity of lanthanide-ion activated $SrWO_4$ phosphors[36] and $CaMoO_4$[37] nanocrystals have been studied.

In this contribution, we report the effect of binary capping agents on the formation of highly uniform, monodispersed and single crystalline β-$NaYF_4$:5 % Tb^{3+}crystals with diverse architectures. We explored the influence of reaction temperature and pH of precursor solution on the morphology of the crystals and their growth mechanism. Additionally, morphology dependent luminescence properties of β-$NaYF_4$: 5 % Tb^{3+} were also studied. To the best of our knowledge, for the first time we investigated the photocatalytic properties of as-prepared β-$NaYF_4$:5 % Tb^{3+} crystals under UV and solar irradiation.

2. Materials and method

2.1 Materials

All the chemicals were of analytical grade and used as-received without any further purification. Yttrium (III) nitrate hexahydrate ($Y (NO_3)_3.6H_2O$) (purity ≥ 99.89%), and terbium(III) nitrate hexahydrate ($Tb (NO_3)_3.6H_2O$) (purity ≥ 99.89%), were purchased from Sigma Aldrich Inc. Sodium fluoride (NaF) and tri-sodium citrate dihydrate ($(Na_3C_6H_5)_7.2H_2O$) were received from Thomas Baker chemicals Pvt. Ltd. N-cetyl-N,N,N,trimethyl ammonium bromide ($C_{19}H_{42}BrN$) was purchased from Loba Chemie Pvt. Ltd. Deionized water was used throughout the experiments.

2.2 Synthesis:

All of the doping ratios of Ln^{3+} are molar in our experiments. In a typical procedure for the preparation of β-$NaYF_4$:5% Tb^{3+} crystals, $Y(NO_3)_3$ and $Tb(NO_3)_3$ (0.2 M) were added into 30 mL of aqueous solution containing 2 mmol of trisodium citrate (0.5882 g) to form the metal-citrate complex. After vigorous stirring for 30 min, 0.1 M of CTAB and 2 M of NaF were introduced into the above solution, respectively. After another agitation for several minutes, the solution was transferred into a stainless steel autoclave with Teflon liner of 80 mL capacity, sealed and heated at 220 °C for 24 h. After that, the autoclave was cooled to room temperature, and the resulting product was separated centrifugally and was washed with distilled water and absolute ethanol. Then, the product was dried under vacuum at 60 °C for 8 h. $NaYF_4$:18 % Yb^{3+},2 % Er^{3+} and $NaYF_4$:18 % Yb^{3+},2 % Tm^{3+} samples were prepared in a manner similar to that for $NaYF_4$:5 % Tb^{3+} sample. Additionally, different hydrothermal treatment temperatures (150 °C, 190 °C and 220 °C) and pH values (3, 7 and 11, 220 °C, 24 h) were selected to investigate the effect of these factors on the morphology, structural and optical properties of the samples. The pH of the mixture was regulated at certain specific values by adding dilute ammonia solution or HCl. Furthermore, control experiments were done in the absence of CTAB or trisodium citrate (either in the presence of CTAB only or trisodium citrate only) respectively to investigate the evolutional process of morphology and structure.

2.3 Characterization techniques

The phase purity and crystallinity of the as-prepared samples were characterized by powder X-ray diffraction (PXRD) using a PANalytical X'PERT PRO instrument and the iron-filtered Cu-Kα radiation (λ = 1.54 Å) in the 2θ range of 10-80° with a step size of 0.02°. To analyze the shape and size of the samples, field emission scanning electron microscopy (FESEM: Hitachi S-4200) was done. Energy-dispersive X-ray analysis (EDXA) of the samples was performed during field emission scanning electron microscopy measurements to obtain the elemental composition of the samples. The specific structure details and morphology were obtained by using FEI Tecnai F30 high resolution transmission electron microscope (HRTEM) equipped with a super-twin lens (s-twin) operated at 300 keV accelerating voltage with Schottky field emitter source with maximum beam current (> 100 nA) and small energy spread (0.8 eV or less). The point-to-point resolution of the microscope is 0.20 nm and line resolution of 0.102 nm with spherical aberration of 1.2 mm and chromatic aberration of 1.4 mm with 70 µm objective aperture size. The powder samples obtained were dispersed in ethanol and then drop-casted on carbon-coated copper TEM grids with 200 mesh and loaded to a single tilt sample holder.

The optical properties of the as-synthesized samples were investigated by a Jasco UV-vis-NIR (Model V570) dual beam spectrometer operated at a resolution of 2 nm. PL spectra were acquired using a Fluorolog Horiba JobinYvon fluorescence spectrophotometer, equipped with a 400 W Xe lamp as an excitation source and a Hamamatsu R928 photomultiplier tube (PMT) as a detector. Lifetime measurements were carried by using an Edinburgh Instruments FLSP 920 system, having a 60 W microsecond flash lamp as the excitation source. Around 30 mg sample was mixed with one ml methanol, made into a slurry and spread over a quartz plate and dried under ambient conditions and introduced into the sample chamber of the instrument prior to luminescence measurements. The UC emission spectra were obtained using an ACTON SP2300 spectrometer attached to a PMT under 980 nm CW diode laser excitations. The photocatalytic activity of β-NaYF$_4$:5 % Tb^{3+} was studied by degradation of dyes in aqueous medium under UV light using a 400 W mercury lamp (λ=200 to 400 nm). All the measurements were performed at room temperature.

3. Results and Discussion

3.1 Structural and morphological investigations:

The composition, crystallinity and phase purity of the phosphors were first examined by XRD. Figure 1 shows, typical XRD patterns of the as-synthesized $NaYF_4$: Ln^{3+} (Ln= Tb, Yb/Er and Yb/Tm). All of the three samples exhibit sharp diffraction peaks that can be indexed to pure hexagonal-phase β-$NaYF_4$ (space group: $P6_3/m$). The full-width at half maxima (FWHM) values of all the reflections are relatively small, suggesting larger crystallite size of the as-prepared samples. The calculated lattice parameters are a =5.9 Å, c =3.5 Å, which is in good agreement with the reported data (JCPDS no. 16-0334). No secondary phase is observed in the XRD patterns, revealing that Tb^{3+}, Yb^{3+}/Er^{3+} and Yb^{3+}/Tm^{3+} have been effectively doped into the β-$NaYF_4$ host lattice. The high crystallinity, as evident by the XRD patterns, is advantageous to the phosphors, as it translates in to less trap centers for photon emission and consequently stronger luminescence.

In general, doping of different lanthanide-ions does not affect the structures and the morphologies of β-$NaYF_4$. Thus, here we studied the effect of external factors on the morphologies of β-$NaYF_4$:5 % Tb^{3+} crystals.

3.2 Effect of reaction temperature:

Temperature plays a critical role in determining the crystalline phase and its morphology. Keeping all the other reaction parameters unperturbed, we investigated the role of the crystal-growth temperatures (150 °C, 190 °C and 220 °C, pH=7) on the crystallinity of the β-$NaYF_4$:5 % Tb particles (Figure 2) which coincides well with the JCPDS No. 16-0334. The noticeable feature was a large difference in the relative intensities of (100), (101), and (201) peaks, indicating the temperature driven preferential orientational growth. The TEM image and FESEM images, in Figure 3 (a) shows that, the β-$NaYF_4$:5 % Tb^{3+} crystals prepared at 150 °C are grown in nearly hexagonal shape and the size is quite polydispersed with average diameter ~2.7 μm and length ~3.1 μm. In comparison, the crystals grown at 190 °C (Figures 3 (b) & (g)) consist of hexagonal microprisms with perfect uniformity, monodispersity, and well-defined crystallographic facets. In TEM image (Figure 3 (b)), regular hexagonal and rectangular particles are observed, which correspond to hexagonal microprisms that are perpendicular and parallel to the copper grids, respectively. The mean diameter and length of particles is estimated to be ~2.5 μm and ~1.7 μm respectively. At temperature 220 °C (Figures 3 (c), 3 (h)), hexagonal microprisms with average diameter ~2.1 μm and length ~2.5 μm are observed, most of them are oriented parallel to the substrate. Moreover, both the tops and bottoms of these microprisms exhibit apparent deep concave centres while the side planes are relatively smoother (Figures 3 (c), 3 (h)). This is because, the growth process occurs at the circumferential edge of each cylindrical β-$NaYF_4$ seed.[38] This also demonstrates that, in this current system, the higher temperature (*i.e.* from 190 to 220 °C) facilitate the longitudinal growth along the <001> direction and elevation in degree of concave structures at the top/bottom surfaces. As we mentioned earlier that, a comparison between the XRD patterns of the β-$NaYF_4$:5 % Tb^{3+} crystals grown at different temperature shows the variation in the relative peak intensities which provides further information on the crystal growth (Figure 2). However, the variation in intensity of XRD peaks can be affected by texturing effect. It should be noted that, the particles prepared at 150 °C are not discussed, because of their non-uniformity and polydispersibility, and thus the FESEM image is also not presented. Based on the above analysis, we reasonably believe that the hydrothermal reaction temperature has significant impact on obtaining the β-$NaYF_4$ microcrystals with uniform morphology and size.

Further, the chemical composition of the β-$NaYF_4$: 5 % Tb^{3+} crystals were characterized by EDXA analysis. As can be seen by Figure 3 (i), all the elements including Na, Y, F and Tb can be detected in the spectrum.

3.3 Effect of pH

Figure 4 compares, the typical XRD patterns of the β-NaYF$_4$: 5 % Tb^{3+} synthesized at different pH values 3, 7 and 11 (temperature 220 °C) which could be indexed to pure hexagonal phase β-NaYF$_4$, but the relative intensities of (100), (110), (101), (200), and (210) peaks are different from each other signifying the possibility of different preferential orientation growth under altered pH conditions. The morphologies of the β-NaYF$_4$: 5 % Tb^{3+} crystallites, (grown at ~220 °C) as a function of pH values, are shown by TEM images in Figure 5. It has been observed that at neutral pH, hexagonal microprisms were formed with average diameter ~2.1 μm and length ~2.5 μm. While, the crystallites obtained at pH=3 are composed of microrods with chipped ends, having average length ~8.7 μm in and diameter ~ 1.1 μm. At pH=11, spindle-like structures were formed with the average length ~3.1 μm and diameter ~2.1 μm. The corresponding SAED patterns (bottom row, Figure 5) reveal that, the crystals are highly single-crystalline in nature. The detailed observations at various pH, was then shown by FESEM images in Figure 6. A very little change in the morphology is observed at pH=9 and 10. On the other hand, the morphology remains almost unchanged at pH=5, while microrods start to form at pH=4. Our study on the effect of pH on morphology of NaYF$_4$ crystals suggest that, the morphology remain unaffected in pH range 5 to 10, while morphology changes below pH=5 and above pH=10. The plausible reason for the modulation in morphology at varied pH is discussed in the next section.

3.4 Formation mechanism of multiform structures

Here, we explain the growth mechanism of formation of hexagonal microprisms based on the cooperative effect of trisodium citrate (TSC) and CTAB. It is well known that the surfaces of a hexagonal prisms are typically {0001} for top/bottom planes and a family of six energetically equivalent $\{10\bar{1}0\}$ prismatic side planes [$(10\bar{1}0)$, $(\bar{1}010)$, $(0\bar{1}10)$, $(01\bar{1}0)$, $(1\bar{1}00)$, and $(\bar{1}100)$] as shown in Figure 7(b).[39] It is widely accepted that, for hexagonal prismatic $NaYF_4$ structures, the citrate ions adsorb at the {0001} facets and thus inhibits the growth at top/bottom planes.[24,25] On the other hand, the detailed observation on the crystal structure of β-$NaYF_4$[40] (Figure 7(d)) revealed that, the density of Y^{3+} on $\{10\bar{1}0\}$ plane is greater, which results in preferential absorption ability of Br^- ions of CTAB at the $\{10\bar{1}0\}$ side planes, similar to the case of gold nanorod formation using CTAB as surfactant.[41,42] Based on FESEM observations (see the supporting information S1.A and B) and above studies, the formation mechanism of β-$NaYF_4$ hexagonal prisms is deduced as follows: In a typical hydrothermal process, trisodium citrate plays dual role of chelating agent as well as structure directing agent. First, at the neutral pH, $H_{3-n}Cit^{n-}$ ions exist as Cit^{3-} and so the chelation between Y^{3+} cations and Cit^{3-} strengthens and thus forms steady Y^{3+}-citrate complexes. This can be confirmed by the formation of white precipitates after the mixing of aqueous solution containing Y^{3+} and trisodium citrate at neutral pH. The strong Y^{3+}-citrate complexes effectively render the slow nucleation and subsequent growth of crystal. Under the hydrothermal conditions, the Y^{3+} -citrate complex would be weakened and Y^{3+} ions would be released gradually. On the other hand, the released Y^{3+} combines with Na^+ and F^- to generate $NaYF_4$ nuclei. During subsequent growth stage, the presence of trisodium citrate inhibits the growth of {0001} facets at top/bottom planes with a relative enhancement of the growth sideways to some degree, whereas, the presence of CTAB tends to just mildly inhibit the $\{10\bar{1}0\}$ side facets. This favors the formation of hexagonal microprisms with well-defined, smooth and sharp edges of prismatic side planes. Conversely, samples prepared by using only CTAB are rod-shaped and when only trisodium citrate is used, the product obtained are still hexagonal prisms; but the edges of prismatic side planes are comparatively not much smoother and sharper as obtained by using CTAB and TSC simultaneously, as shown by arrows in Figure S1.B.

Further, the formation of microrods and spindle-like structures at varied pH are presented in Figure 7 (a-c) and is explained as follows: if the pH value of the solution is changed, the existing form of Cit^{3-} changes to $HCit^{2-}$, H_2Cit^{-}, or H_3Cit, and the chelation between $H_{3\_n}\,Cit^{n-}$ and the Y^{3+} ions are affected. Moreover, at different pH values, the ability of Cit^{3-} to adsorb on certain crystal facets is different from each other, leading to the differential growth rate of crystal facets, which results in the formation of anisotropic geometries.[20] In acidic pH, Cit^{3-} anions are not able to bind selectively and effectively on {0001} facets, rather possibly bind to $\{10\bar{1}0\}$ facets of growing β-$NaYF_4$ crystallites, and therefore, allow the particles to grow along [0001] direction leading to the formation of 1-D prismatic microrods. It is worth mentioning here that, CTAB is known to play a role to form gold nanorods by binding at {100} and {110} planes in acidic pH.[43] While in alkaline environment, the existent form of Cit^{3-} is not affected, rather Cit^{3-} ions adsorb strongly on to the {0001} surfaces and promote the growth more prominently along the side directions forming spindle-like strictures. However, the effect of CTAB on crystal morphology at basic pH is not very clear to us.

3.5 UV-visible studies

The UV-vis absorption spectra of β-$NaYF_4$:5 % Tb^{3+} (Figure S2) shows a strong absorbance peak at ~253 nm, indicating large band gap of β-$NaYF_4$:5 % Tb^{3+} followed by a broad absorbance above ~400 nm onwards. The optical band gap was determined by Tauc plot as shown in Figure 8. The band-gap for the as-prepared β-$NaYF_4$:5 % Tb^{3+} was calculated to be ~5.6 eV. Surprisingly, a new and strong energy level was observed, with an absorption edge at ~3.2 eV, which might be due to the Tb^{3+} doping in the host lattice and a strong function of doping concentration.[44]

3.6 Photoluminescence studies

A. *β*-$NaYF_4$:Tb^{3+}

Owing to the non-existence of d electrons in Y^{3+} ([Kr] $4d^0$) in un-doped $NaYF_4$, the probability of emission is negligible in the host matrix. Figure 9 compares, the excitation (a) and emission (b) photoluminescence spectra of microrods, hexagonal microprisms and spindle-shaped Tb^{3+} ion-doped $NaYF_4$ crystals. It can be evidently seen that, in all the three samples the peak-positions in excitation and emission spectra remain similar, and the bands differ only in their relative intensities. The excitation spectrum monitored at λ_{ex}=544 nm, consist of the characteristic *f-f* transition lines within the Tb^{3+} $4f^8$ configuration. The excitation lines can be assigned to the transition from $^7F_6$ ground state to the different excited states of Tb^{3+}, so as at, ~288 nm ($^5I_6$), ~306 nm ($^5H_6$), ~321 nm ($^5D_0$), ~344 nm ($^2G_3$), ~356 nm ($^5D_2$), ~372 nm ($^5G_6$), and ~383 nm ($^5D_3$), respectively. The obtained emission spectra monitored at λ_{ex} = ~375 nm, yielded weak blue and intense green emissions in the regions of 400-450 nm and 480-680 nm respectively, which are due to the $^5D_3 \rightarrow {}^7F_J$ (J = 3, 4, 5, 6) and $^5D_4 \rightarrow {}^7F_J$ (J = 3, 4, 5, 6) transitions of Tb^{3+} ions, respectively. Specifically, the emission bands at ~414 and ~436 nm are attributed to the emission transitions of $^5D_3 \rightarrow {}^7F_5$ and $^5D_3 \rightarrow {}^7F_4$ respectively. Four prominent emission peaks centered at ~488, ~544, ~584, and ~619 nm, originates from the transitions of $^5D_4 \rightarrow {}^7F_6$, $^5D_4 \rightarrow {}^7F_5$, $^5D_4 \rightarrow {}^7F_4$, and $^5D_4 \rightarrow {}^7F_3$ respectively.[45] Among these transitions, the green emission $^5D_4 \rightarrow {}^7F_5$ at ~544 nm is the most intense emission, which corresponds to a magnetic dipole transition.

The optical properties of inorganic materials are strongly dependent on their size, morphology, doping, crystallinity and other parameters, that affect its band structure. We observed that under similar measurement conditions, the microrods possess highest emission intensity, while spindle-like structures have lowest emission intensity. The relative intensity of hexagonal microprisms lies in between microrods and spindle-like structures. The difference in relative intensities might occur due to the difference in the effects of crystal field perturbation on individual *f-f* transition, as a consequence of the different morphologies and size of the samples.[46] The other reason might be, the difference in surface area of different facets, as in an anisotropic material, the interaction with light and photon emission also get influence by the material crystallinity and exposed facets. Large surface area also introduces larger number of defects into the phosphor crystal. Defects may quench the luminescence intensity of phosphors by non-radiative recombination in electrons and holes. Thus, the phosphor with reduced surface area would show improved PL intensity.[47] Herein, we believe that, the microrods possessed smallest and spindle-like structures possessed largest surface area based on results obtained by PL decay studies. Moreover, the SAED pattern of microrods in Figure 5 (d), showed highest crystallinity, thus lesser defects and highest luminescence intensity.

The PL decay curves for the luminescence of Tb^{3+} in β-$NaYF_4$:5 % Tb^{3+} are shown in Figure 10. These curves can be well fitted by a single exponential function as $I(t) = I_0 \exp(-t/\tau)$ where, I_0 is the initial emission intensity at t=0, τ is the 1/e lifetime of the emission centre. The lifetimes for $^5D_4$ were detected at 544 nm for $^5D_4 \rightarrow {}^7F_5$ transition of Tb^{3+} by excitation at 375 nm and were determined to be 4.39 ms, 4.10 ms and 4.09 ms for microrods, hexagonal microprisms and spindle- like structures respectively (Figure 10). The lifetime values and fitted parameters for different samples are listed in Table 1. The variation in luminescence lifetimes is consistent with that of emission spectra. Spindle-like structures showed lowest luminescence lifetime. This infers that, they possess largest surface area, because heavy non-radiative transitions at larger surfaces lead to shortest luminescence lifetime.[48] Consequently, on the basis of lifetime dependence on surface area, we confirm that spindle- like structures possess largest surface area; tend to shortest luminescence lifetime and lowest luminescence intensity and the vice-versa for microrods.

The varying luminescence intensities for different morphologies of β-NaYF$_4$:5 % Tb^{3+} are also represented by CIE chromaticity diagram as shown in Figure12. The CIE coordinate values for the emission spectrum of β-NaYF$_4$:5 % Tb^{3+} are determined as x=0.2690, y=0.4692 (microrods), x=0.3256, y=0.5277 (hexagonal microprisms) and x=0.3091, y=0.4838 (spindle-like structures), located in the green region.

B. β-NaYF$_4$:Yb^{3+}/Er^{3+}:

Figure 11 (a) shows, the upconversion luminescence spectra of Yb^{3+}, Er^{3+}- co-doped β-NaYF$_4$ hexagonal microprisms, under 980 nm NIR laser excitation. The spectra display four distinct Er^{3+} emission bands. The emission peak at ~408 nm is assigned to transition from $^2H_{9/2}\rightarrow{}^4I_{15/2}$. The emission peaks at ~521 and ~540 nm in the green region are assigned to transitions from $^2H_{11/2}$ and $^4S_{3/2}$ to $^4I_{15/2}$. The red emission peak at ~655 nm results from $^4F_{9/2}$ to $^4I_{15/2}$ transition. The CIE coordinate values for the emission spectrum of β-NaYF$_4$:Yb^{3+}/Er^{3+} are determined as x=0.2805, y=0.6836, located in green region as shown in Figure 12.

C. β-NaYF$_4$:Yb^{3+}/Tm^{3+}:

Figure 11 (b) shows the up-conversion luminescence spectra of Yb^{3+}, Tm^{3+}- co-doped β-NaYF$_4$ hexagonal microprisms under 980 nm NIR laser excitation. The spectra show four distinct emission lines of Tm^{3+}. The emission peaks at ~450 and ~646 nm are assigned to transitions from $^1D_2$ and $^1G_4$ to $^3F_4$. The emission peaks at ~475 and ~804 nm are results from $^1G_4$ and $^3H_4$ to $^3H_6$ transition. The CIE coordinate values for the emission spectrum of β-NaYF$_4$:Yb^{3+}/Tm^{3+} are determined as x=0.1286, y=0.0840, located in blue region as shown in Figure 12.

3.7 Photocatalytic Studies

Photocatalytic measurements were performed by exposing β-NaYF$_4$:5 % Tb^{3+} phosphors to the irradiation of a 400 W mercury lamp (λ=200 to 400 nm). Because of the presence of broad absorption above ~400 nm onwards (Figure S2) and the additional inter-band energy level in β-NaYF$_4$:5 % Tb^{3+} as shown in Figure 8 (discussed earlier in section 3.5), it was tested for the photocatalytic properties under UV irradiation. The presence of inter-band energy level, accelerates the interfacial electron transfer process, and thus facilitates photocatalysis reaction in visible and ultraviolet light irradiation as demonstrated by Xie *et.al*., in Ce$_x$Ti$_{(1-x)}$O$_2$.[49] To study the photoselectivity of β-NaYF$_4$:5 % Tb^{3+} phosphors, we studied the degradation behavior of four different dyes namely, methyl orange (MO), methylene blue (MB), rhodamine B (RhB) and malachite green (MG). The sample suspensions were kept in dark overnight to reach the equilibrium. The UV-visible absorbance spectra for degradation of different dyes using β-NaYF$_4$:5 % Tb^{3+} are compared in Figure 13. The degradation of dyes was observed through reduction in absorbance peak intensity with an increase in the irradiation time. The kinetics of the reaction was plotted as (C/C_0) against time (t), where C_0 is the initial concentration and C is the final concentration of different dyes (Figure 14 and 15 (a)). The characteristic absorbance peaks of MB, RhB, MO, and MG were found at λ= ~662 nm, ~555 nm, ~463 nm, and ~617 nm, respectively, which were used as references for photocatalytic degradation for respective dyes. Following the exposure, the degradation of all dyes was negligible in the absence of β-NaYF$_4$:5 % Tb^{3+}phosphors which are shown by the control dye analysis (Figure 14). The β-NaYF$_4$:5 % Tb^{3+} phosphors degraded 11 %, 14 %, 28 % and 92 % of MO, MG, RhB and MB respectively within 320 min of UV irradiation (Figure 14). In addition, we also investigated the photocatalytic activity of MB under sunlight irradiation, which showed 80 % degradation efficiency (See the supporting information Figure S3). It is clear that, RhB degraded to some extent and MB decomposed dramatically during the irradiation period. However, the absorption lines of other two dyes MO and MG are hardly affected (Figure 15 (a)). One probable reason for selectivity for RhB is that, the emission of β-$NaYF_4$:5 % Tb^{3+} locates in green region (540-570 nm) which overlaps with the absorption of rhodamine B. We believe that, the highest selectivity for MB is might be due to its molecular structure. According to previous studies, –CH_3 elimination and C-N cleaving can certainly occur in MB molecules via formation of $OH^{\cdot}$ radical.[50] The plausible mechanism involved in degradation of MB is as follows: Upon irradiation, the photon absorption leads to formation of a hole (h^+) in the valance band and electron (e^-) in conduction band.[51] The hole oxidizes water molecules to produce hydroxyl radicals (OH^-), whereas the electron in the conduction band reduces the oxygen adsorbed on the particles to O^{2-}. The active oxygen and radical species such as OH^- and O^{2-} degrade the MB dye molecules by directly cleaving the aromatic ring at azo bond and forming various by-products such as carbon dioxide, water, nitrate, sulphate and ammonia[52] as represented as scheme in Figure 16.

Extensive studies on photocatalysts have demonstrated that, the size and shape of particles profoundly affect their activity as the photocatalytic reactions are typically surface-based processes.[53] These facts enthuse us to check-out, the morphology dependent photocatalysis studies of our samples. The photo-selectivity studies were performed with hexagonal prism-shaped crystals, and then the degradation of MB was compared with the as-prepared microrods and spindle-like structures to study the morphological dependence on photocatalytic activity. The photocatalytic results as shown in Figure 15 (b) indicate that, 92 % of MB molecules degraded by hexagonal prism shaped crystals, while 82 % and 71 % MB dye degraded by spindle-like structures and microrods respectively in 320 min. Additionally, it is observed that although hexagonal prisms showed highest degradation after complete reaction, but in the initial and intermediate period, *i.e.* after 80 min and 200 min, spindle shaped particles showed highest degradation (64 % and 75 %) as compare to hexagonal prisms (21 % and 64 %) and microrods (53 % and 57 %). The initial higher degradation by spindle shaped particles may be attributed to their larger surface area. From luminescence studies, we assume that spindle like structures have larger and microrods have smaller surface area. Moreover, FESEM images show the greater roughness of spindle like structures. Photocatalysis results are well consistent with PL and FESEM observations. The larger surface area and roughness of spindle like structures provide more catalytic active sites, thus showed greater degradation initially. This is because, it has been well documented that, larger surface area consist of low-coordinated atoms located in the defects such as edges, kinks, and vacancies which offers more active sites.[54] Microrods with lowest surface area showed lowest degradation performance. But at this stage, it cannot be fully understood that, why β-$NaYF_4$:5 % Tb^{3+} hexagonal prisms showed highest degradation efficiency (92 %) after complete reaction of 320 min. We believe that, this might be due to well-defined highly crystalline facets of hexagonal prism shaped crystals (Figure 5 and 6). It has been demonstrated that, the surface atoms of different facets have unique coordination environment and different surface energies yielding, different and distinct catalytic properties.[54] Our group have also previously demonstrated the enhanced photocatalytic activity of {001} faceted BiOCl crystals.[55] Therefore, the facets of hexagonal prisms with high surface energies might have exposed, that could have increased the number of catalytic active sites, which in turn, might have rendered enhanced photocatalytic degradation of MB. More interestingly, it has also been observed that, in case of degradation by microrods and spindle-like structures, the absorption peak diminished as well as gets broadened and showed hypsochromic effect with increasing time (See supporting information Figure S4). The absorption peak of MB shifted by ~12 nm (*i.e.* from 662 nm to 550 nm) towards lower wavelength with increasing time. This blue shift may be attributed to oxidized MB by formation of demethylated dye, resulting from Ndemethylation of dimethylamino group in MB that occurs concomitantly with oxidative degradation.[56]

4. Conclusion

In summary, hexagonal phase of $NaYF_4$: Ln^{3+} (Ln=Tb, Yb/Er and Yb/Tm) microcrystals with multiform morphologies were successfully synthesized via cationic/anionic binary capping agent system: CTAB and trisodium citrate-assisted hydrothermal route. Under UV excitation, the as-prepared β-$NaYF_4$: 5 % Tb^{3+}crystals emit strong green emission (down-conversion luminescence) and possess long luminescence lifetime in milliseconds. In contrast, under 980 nm NIR excitation, the Yb/Er- and Yb/Tm-co-doped $NaYF_4$ samples exhibit strong green and blue up-conversion luminescence, respectively. The experimental results indicate that, the luminescence properties of the β-$NaYF_4$: 5 % Tb^{3+} phosphors are strongly dependent on their crystalline size and shape. The photocatalytic studies showed that, β-$NaYF_4$: 5 % Tb^{3+} phosphors are highly selective for MB. In addition, we have also discussed the correlation between the morphologies and photocatalytic activities. To the best of our knowledge, for the first time, we have studied the photocatalytic selectivity and morphology dependent effects in catalytic activity of lanthanide- ion doped rare earth fluoride crystals. Apart from their photocatalytic properties, the unique luminescence properties and controlled morphologies of these phosphors may endow potential applications in field of color displays, light-emitting diodes (LEDs) and solid state lasers.

Acknowledgement

Pankaj Poddar acknowledges the Centre for Excellence in Surface Science at the CSIR-National Chemical Laboratory, and network project Nano-Safety, Health & Environment (SHE) funded by the Council of Scientific and Industrial Research (CSIR), India, and the

Department of Science & Technology (DST), India through and Indo-Israel grant to develop materials for solar-voltaic energy devices (DST/INT/ISR/P-8/2011). Preeti Padhye acknowledges the support from the University Grant Commission (UGC) for providing the Senior Research Fellowship. Preeti Padhye acknowledges Dr. Vineet Kumar Rai, Riya Dey, Laser and Spectroscopy laboratory, Department of Applied Physics, ISM, Dhanbad, for up-conversion luminescence measurements and Dr. V. Sudarshan, Chemistry division, Bhabha Atomic Research Centre, Mumbai, for luminescence lifetime measurements.

Table 1: Luminescence lifetime values of *β*-$NaYF_4$: 5 % Tb^{3+} with different shapes.

Sample	**τ (ms)**	**χ^2**
Microrod	4.39	1.78
Hexagonal microprism	4.10	1.72
Spindle-like structure	4.09	1.67

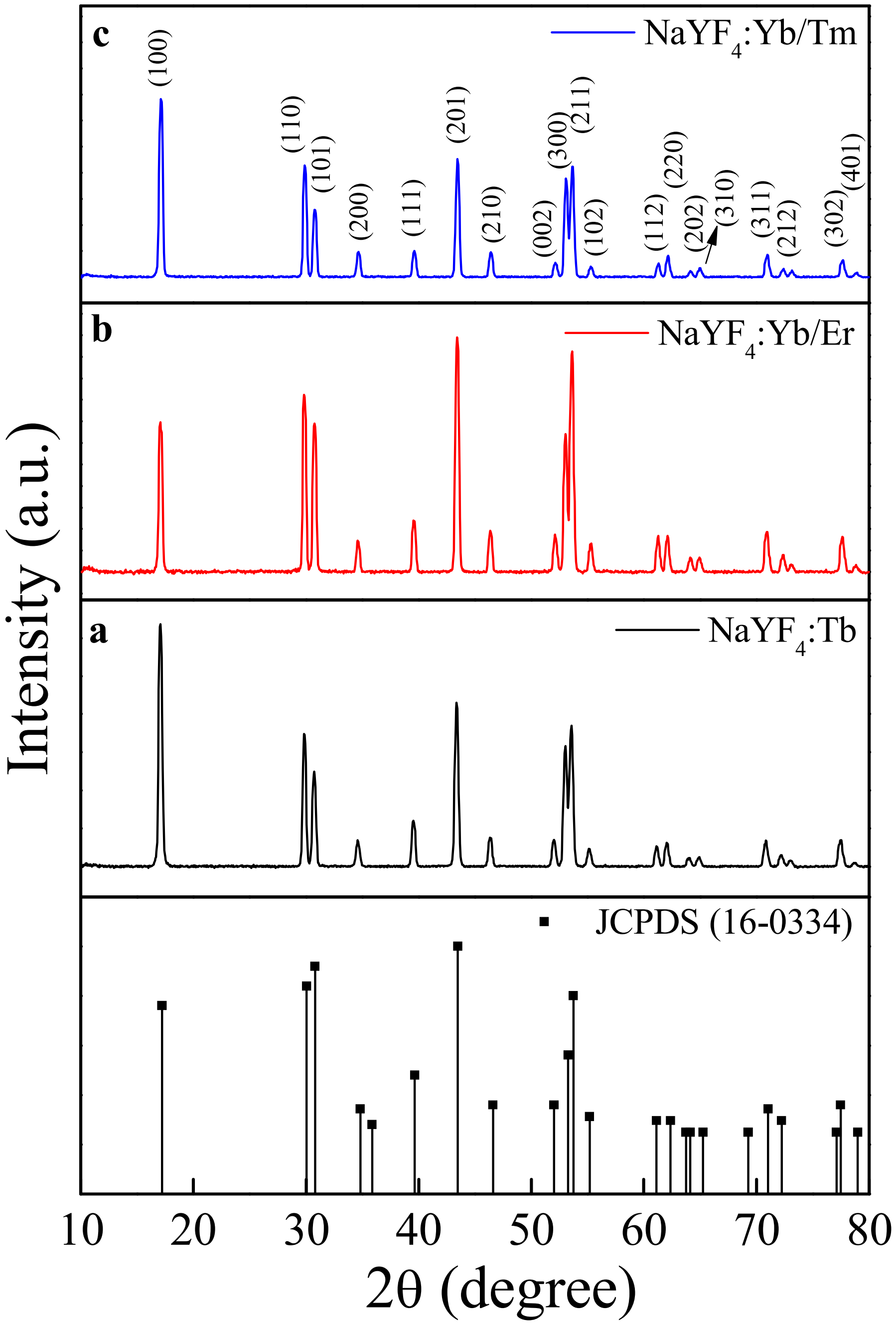

Figure 1: The XRD patterns for the as-prepared (a) $NaYF_4$:5 % Tb^{3+}, (b) $NaYF_4$: 18 % Yb^{3+}/2 % Er^{3+}, (c) $NaYF_4$: 18 % Tb^{3+}/2 % Tm^{3+}.

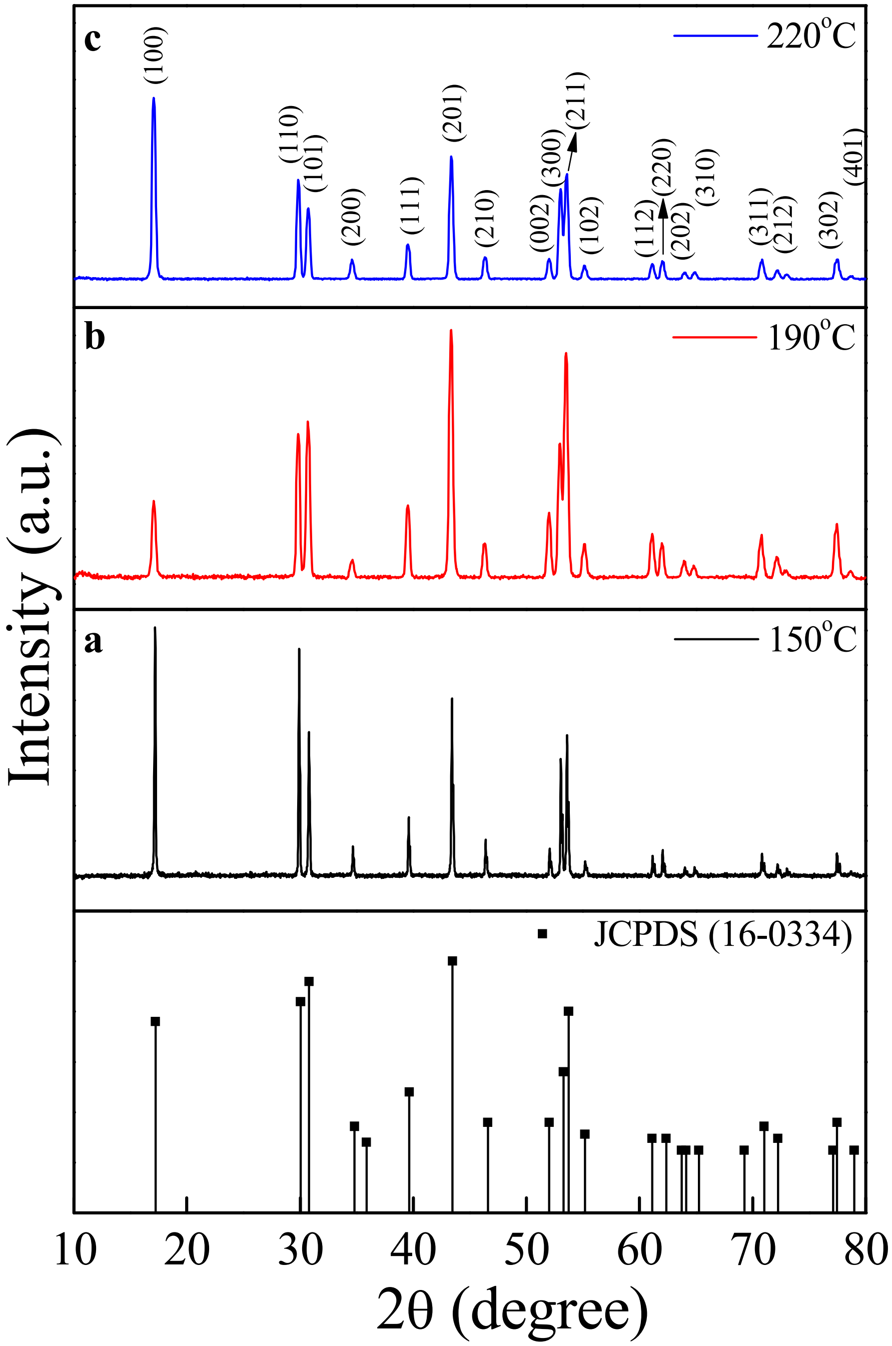

Figure 2: The XRD patterns of β-NaYF$_4$: 5%Tb^{3+} prepared at different temperatures (a) 150 °C, (b) 190 °C, (c) 220 °C and the standard data of hexagonal β-NaYF$_4$ (JCPDS- 16-0334) as a reference.

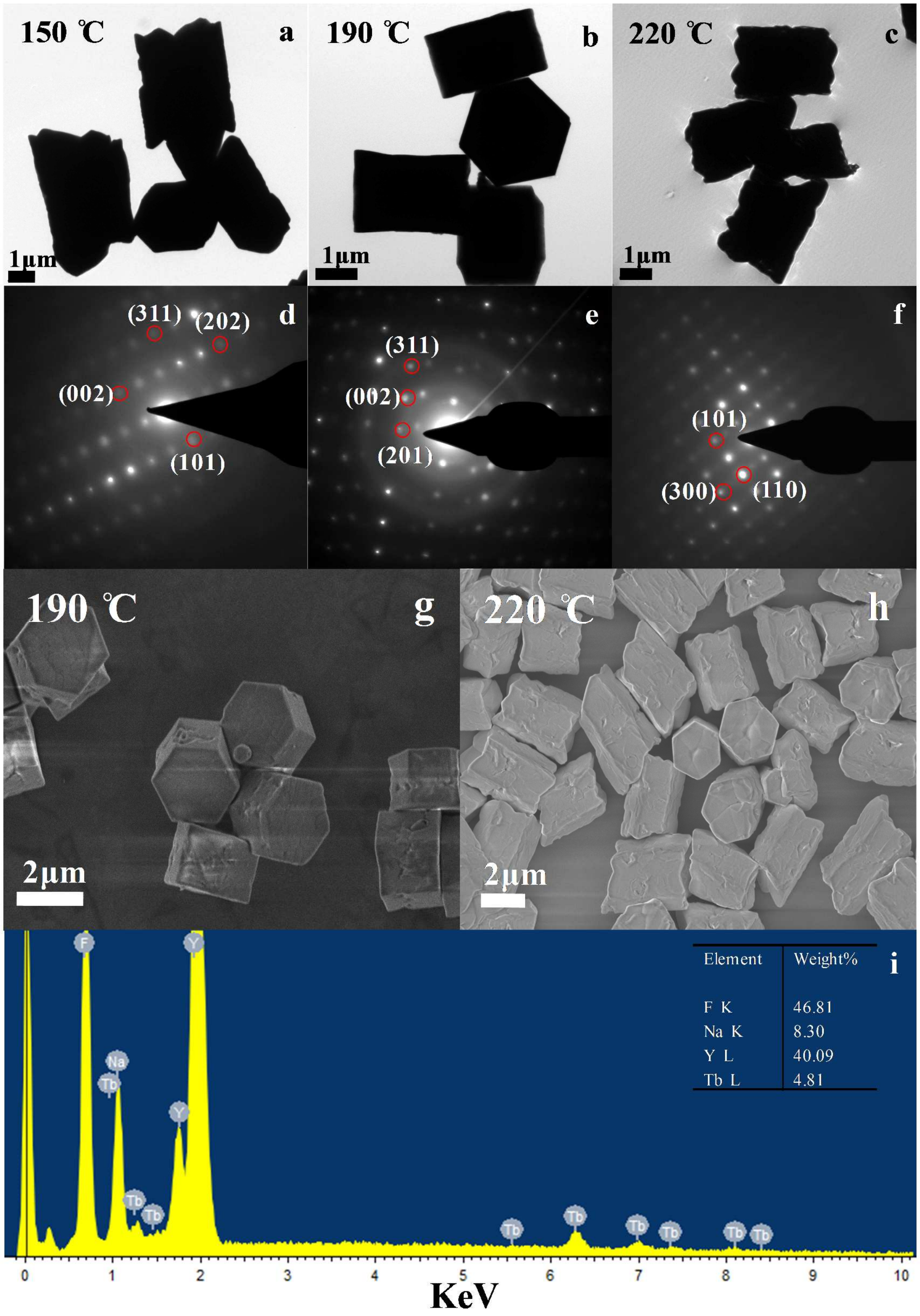

Figure 3: TEM images in the top row shows the influence of the synthesis temperature on the shape of β-NaYF$_4$: 5 % Tb^{3+} crystals ((a) 150 °C, (b) 190 °C, (c) 220 °C). The middle row

shows corresponding SAED patterns in the same order. The FESEM images in the bottom row shows, the change in morphology of β-NaYF$_4$: 5 % Tb^{3+} crystals prepared at (g) 190 °C and (h) 220 °C. (i) Energy-dispersive X-ray analysis (EDXA) patterns of β-NaYF$_4$: 5 % Tb^{3+} crystals.

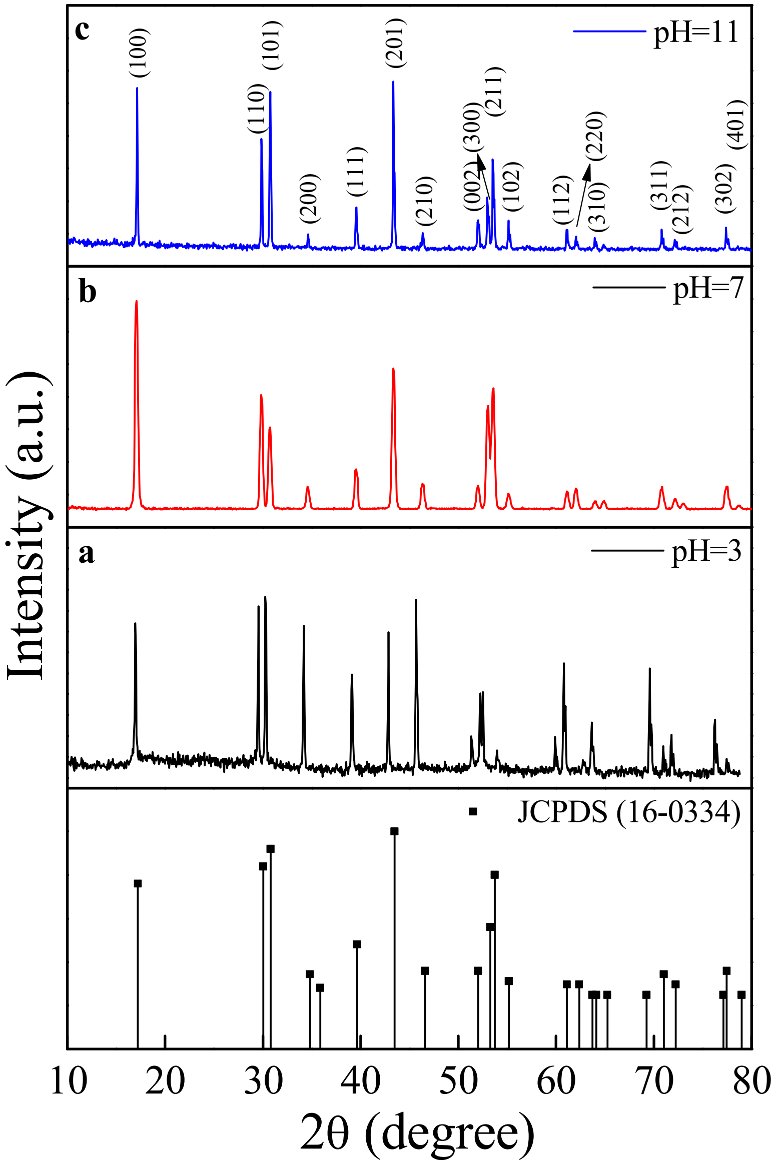

Figure 4: The XRD pattern of β-NaYF$_4$: 5 % Tb^{3+} at different pH values of solution (a) pH=3, (b) pH=7, (c) pH=11 and the standard data of hexagonal β-NaYF$_4$ (JCPDS-16-0334) as reference.

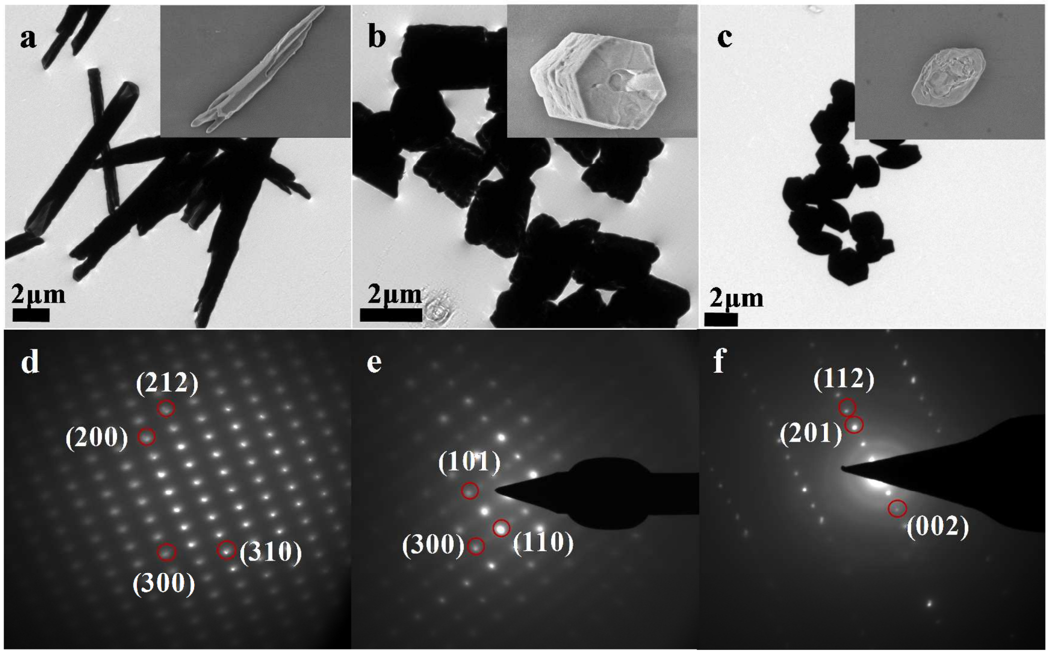

Figure 5: TEM images showing influence of pH on the shape of β-NaYF$_4$: 5 % Tb^{3+} crystals. (a) Prismatic microrods with chipped ends obtained at pH=3. (b) Hexagonal microprisms at pH=7. (c) Spindle-like crystals at pH=11. The images in insets show the zoom view of the corresponding FESEM images for the sake of comparison. (d, e, f) showing corresponding SAED patterns.

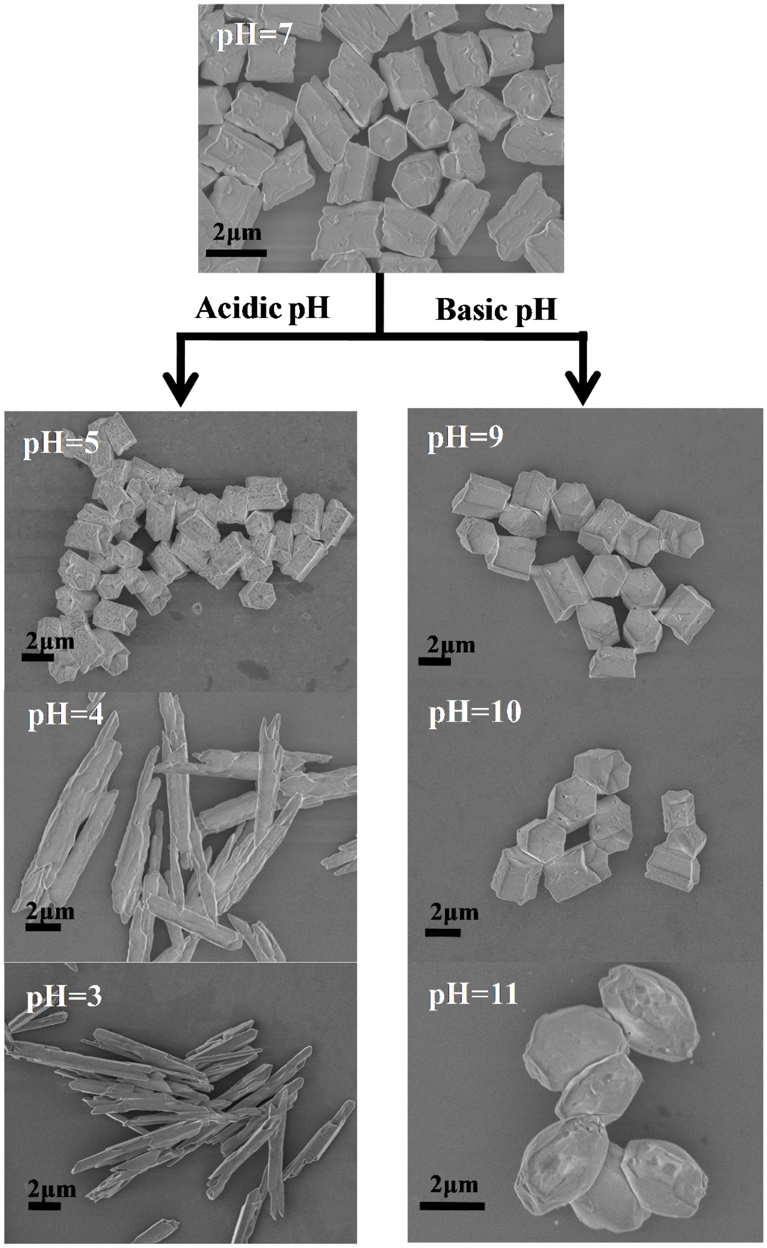

Figure 6: FESEM images showing influence of pH on the shapes of β-NaYF$_4$: 5 % Tb^{3+} microcrystals.

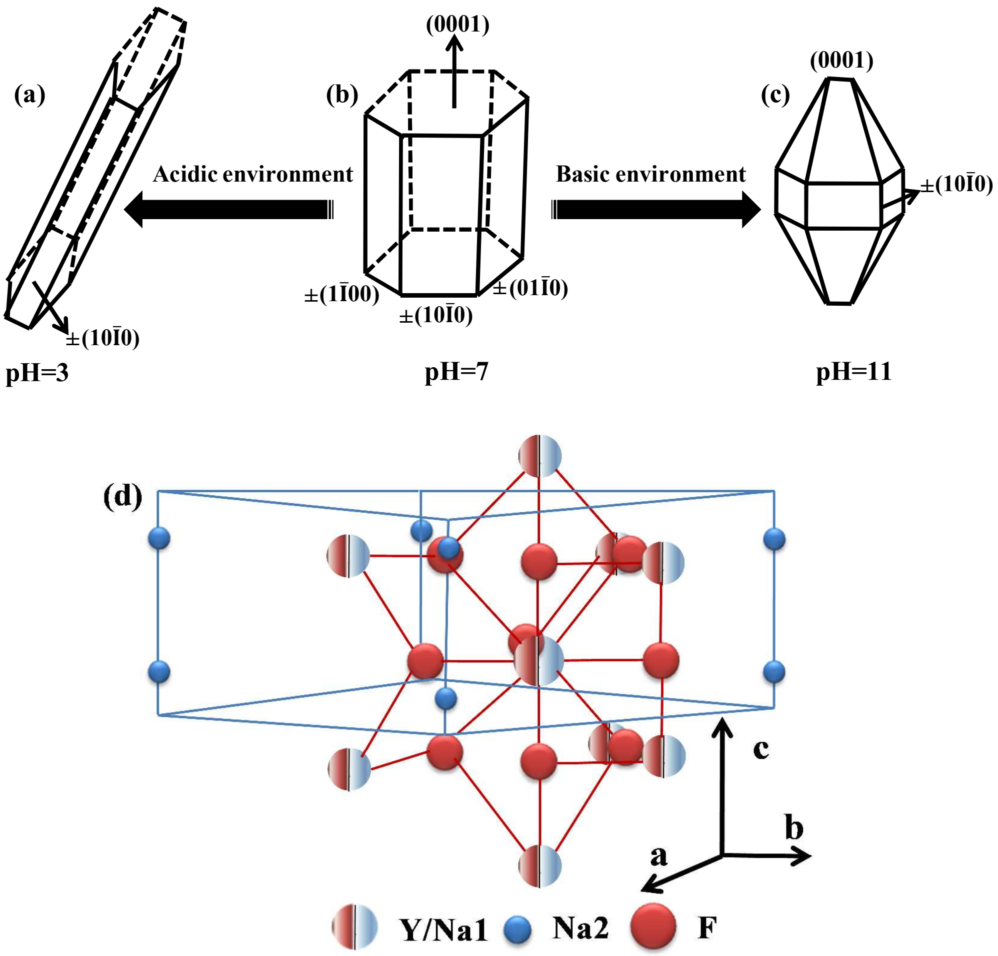

Figure 7: Schematic diagram showing the effect of pH (a-c) on the morphology, (b) the anisotropy of the β-NaYF$_4$ crystal, and (d) schematic presentation of hexagonal phase β-NaYF$_4$ crystal structure (reference 40).

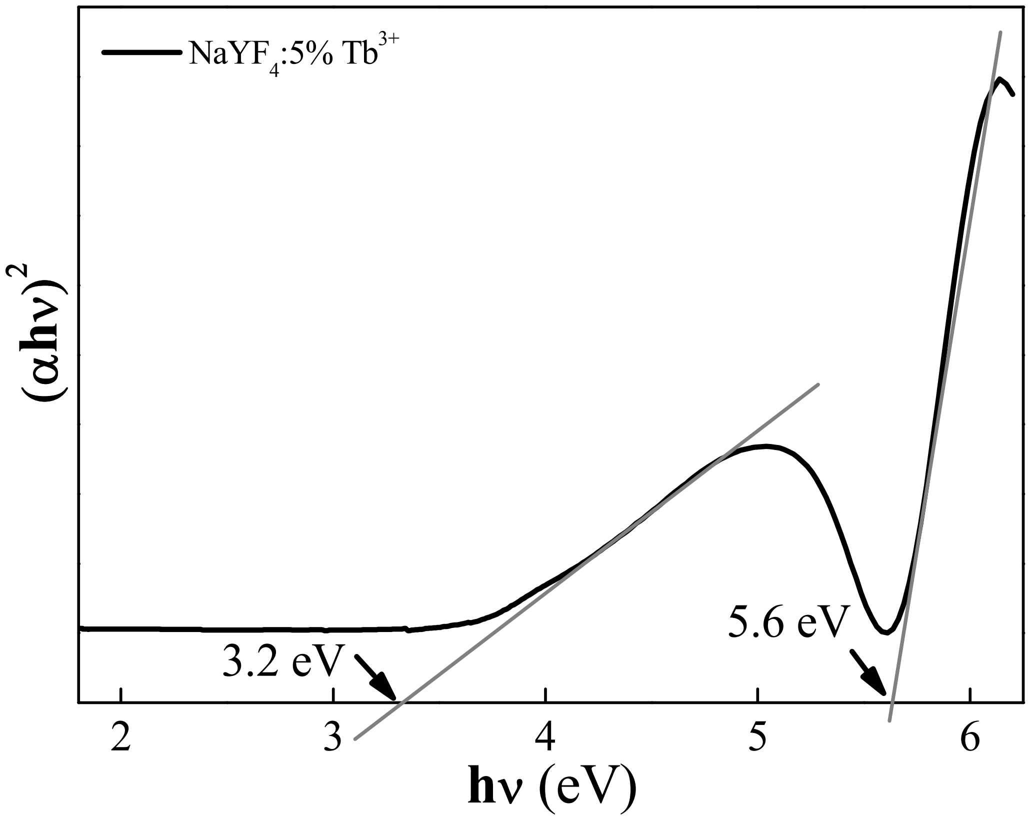

Figure 8: Tauc plot for the estimation of optical band gap energy of β-NaYF$_4$:5 % Tb^{3+}.

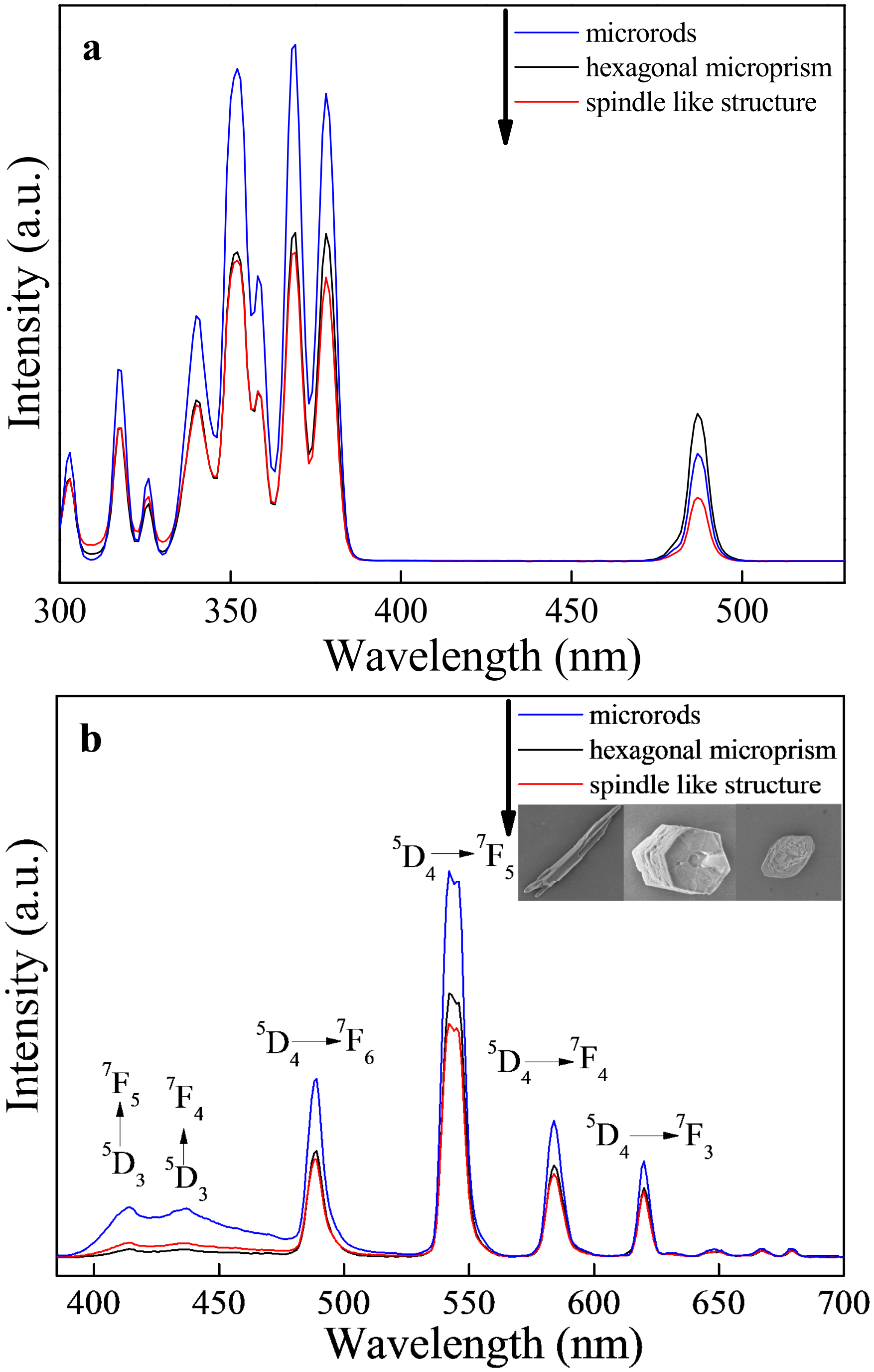

Figure 9: A comparison of static photoluminescence (a) excitation spectra at λ_{em}= 544 nm, and (b) emission spectra at λ_{ex}= 375 nm of β-NaYF$_4$:5 % Tb^{3+} crystals with different shapes.

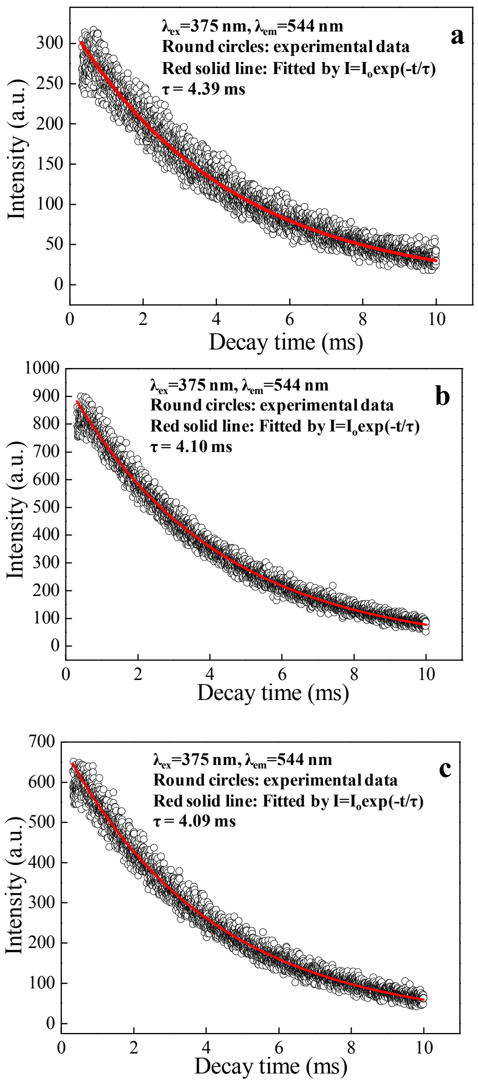

Figure 10: The luminescence decay curves for the $_5D^4\rightarrow_7F^5$ emission of Tb^{3+} (λ_{ex}=375 nm, λ_{em}=544 nm) in β-$NaYF_4$:5 % Tb^{3+} with different morphologies: (a) microrods, (b) hexagonal microprisms, (c) spindle-like structures. The fitted lifetime values are indicated inside the figures.

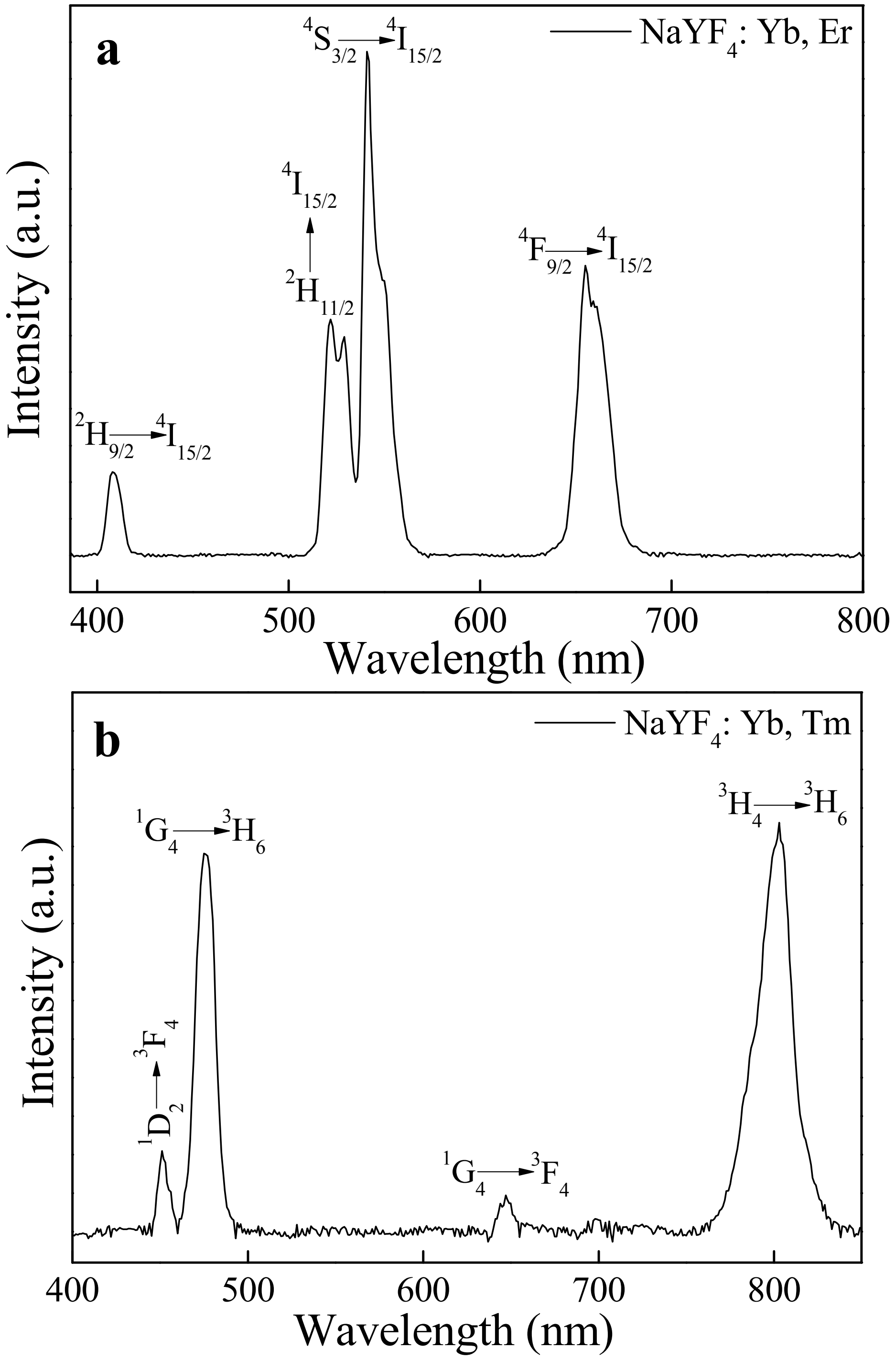

Figure 11: Upconversion emission spectra of (a) $NaYF_4:Yb^{3+}/Er^{3+}$ and (b) $NaYF_4:Yb^{3+}/Tm^{3+}$ hexagonal microprisms under 980 nm laser excitation.

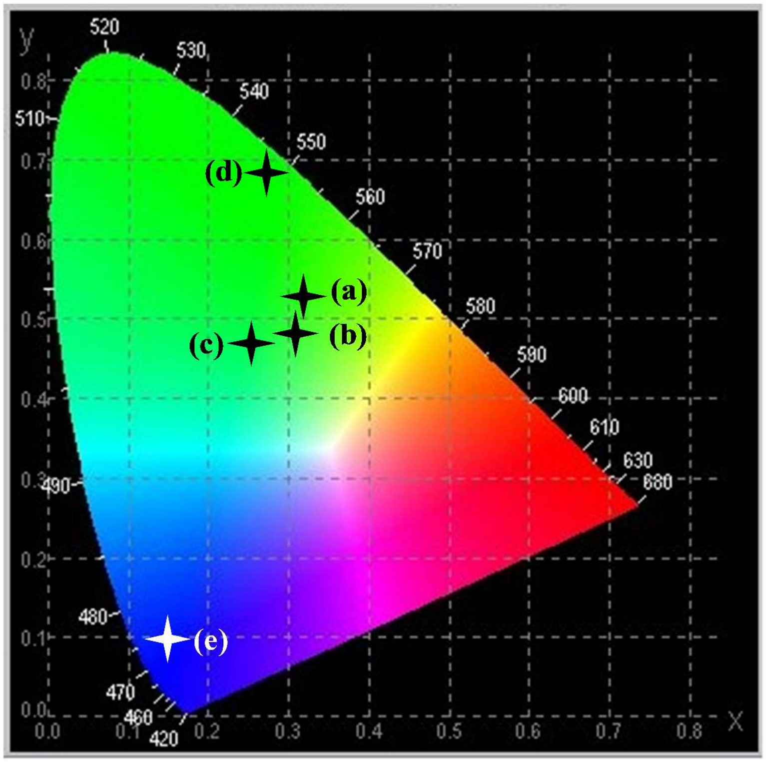

Figure 12: CIE chromaticity diagram showing the emission colors for (a) β-NaYF$_4$:5 % Tb^{3+} at pH=7, (b) β-NaYF$_4$:5 % Tb^{3+} at pH=11, (c) β-NaYF$_4$:5 % Tb^{3+} at pH=3, (d) β-NaYF$_4$:Yb^{3+}/Er^{3+}, (e) β-NaYF$_4$:Yb^{3+}, Tm^{3+}.

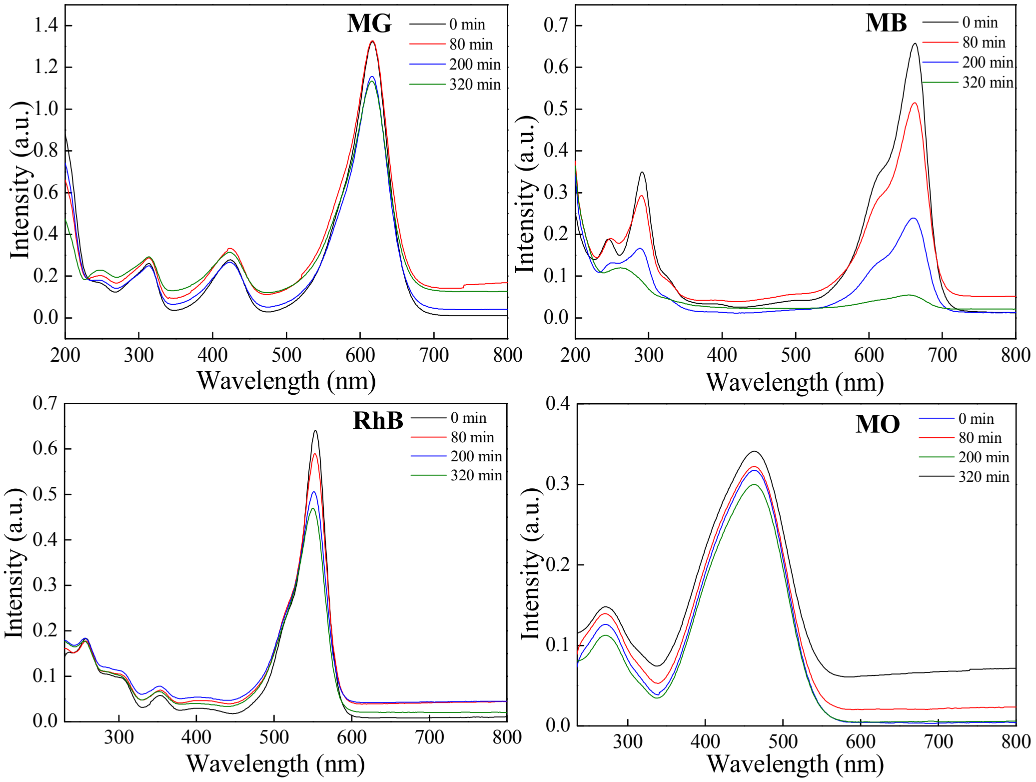

Figure 13: Photocatalytic selectivity of *β*-$NaYF_4$:5 % Tb^{3+} for different dyes: malachite green, methylene blue, rhodamine-B, and methyl orange, under irradiation of 400 W mercury lamp for 320 min.

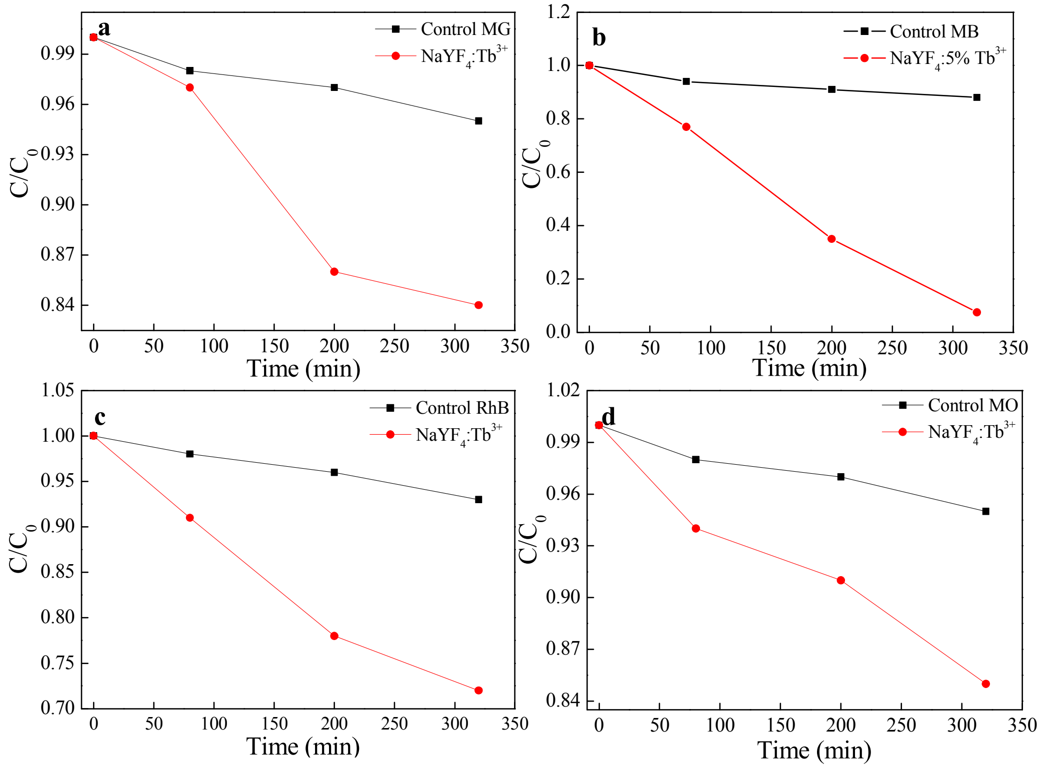

Figure14: Plots of dye concentrations (*C/C₀*) vs. time showing photodegradation of different dyes: (a) MG, (b) MB, (c) RhB, and (d) MO, under irradiation of 400 W mercury lamp for 320 min.

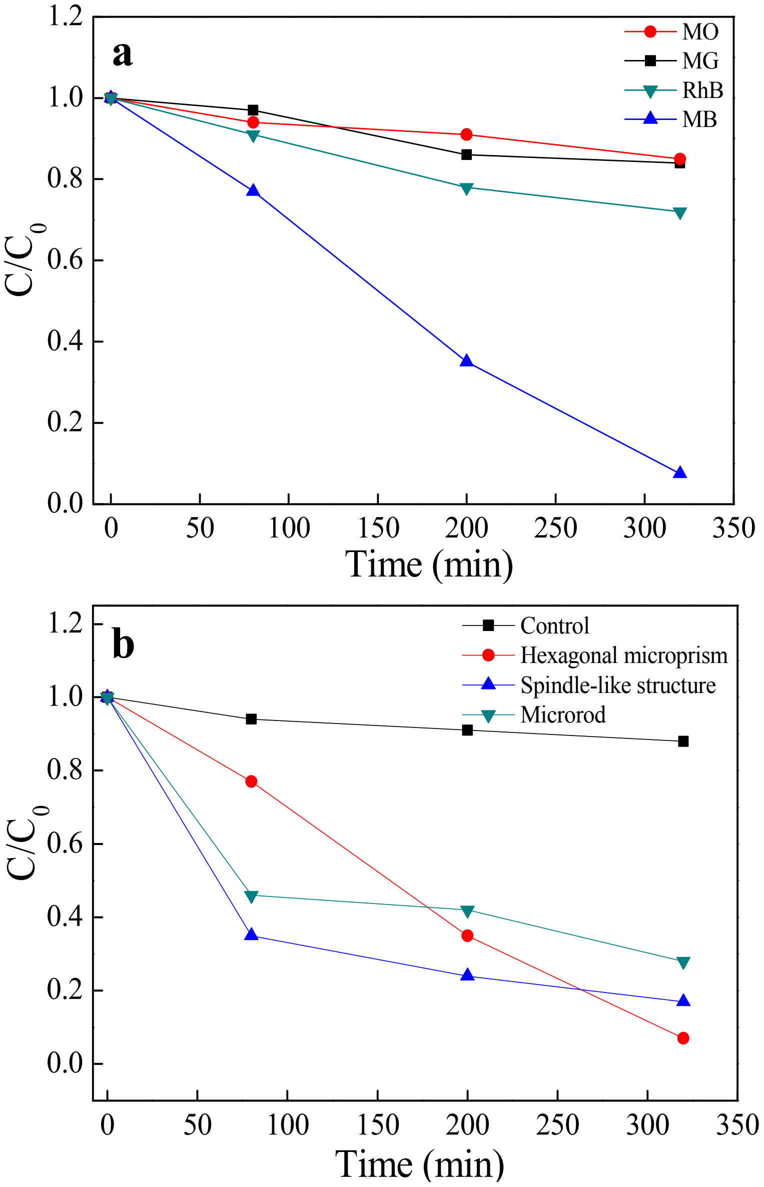

Figure15: Plots of dye concentrations (*C/C_0*) vs. time showing comparison of (a) photodegradation of different dyes: MO, MG, RhB and MB with hexagonal prisms and (b) photodegradation of MB using β-$NaYF_4$:5 % Tb^{3+} with different shapes, under irradiation of 400 W mercury lamp.

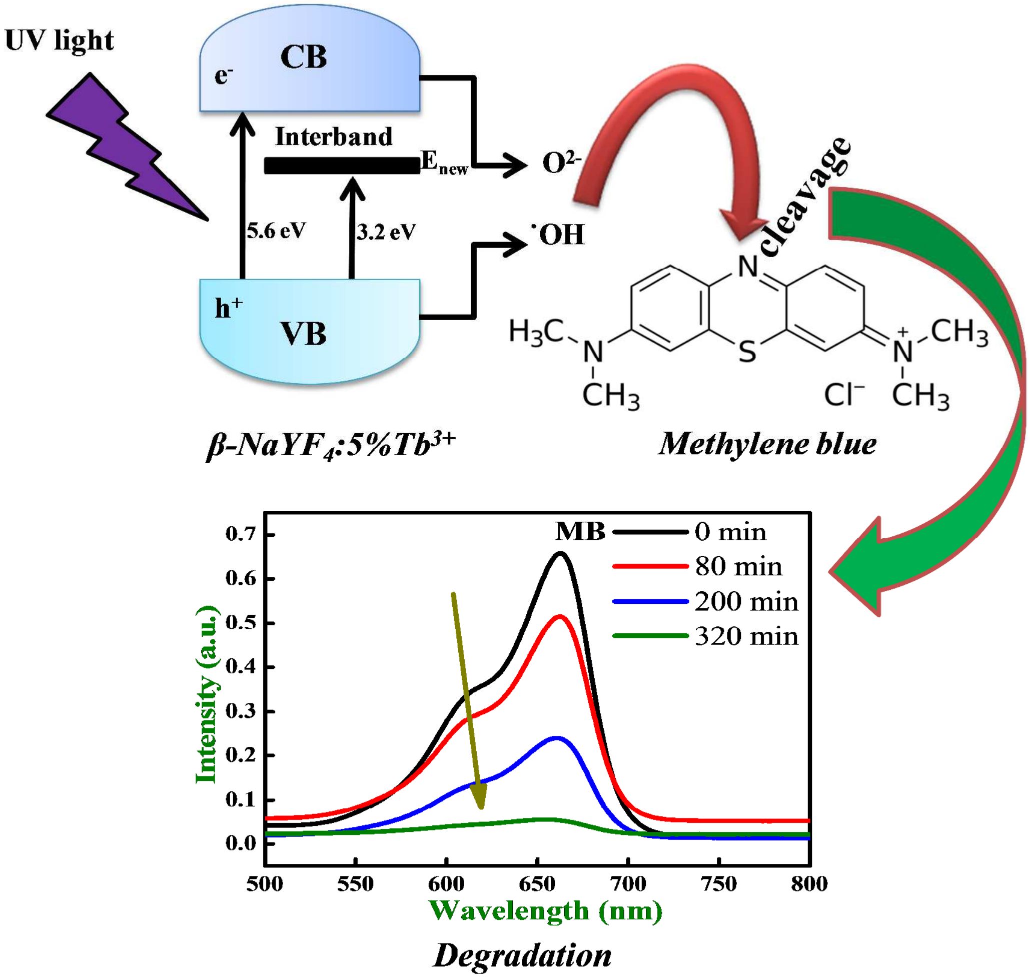

Figure 16: Schematic representation for the photocatalysis mechanism of methylene blue in presence of β-NaYF$_4$:5 % Tb^{3+} crystals.

TOC Graphic

Optical and photocatalytic properties of uniform and monodispersed *β*-NaYF$_4$:5%Tb^{3+} phosphor crystals with multiform morphologies fabricated via binary capping agent assisted system

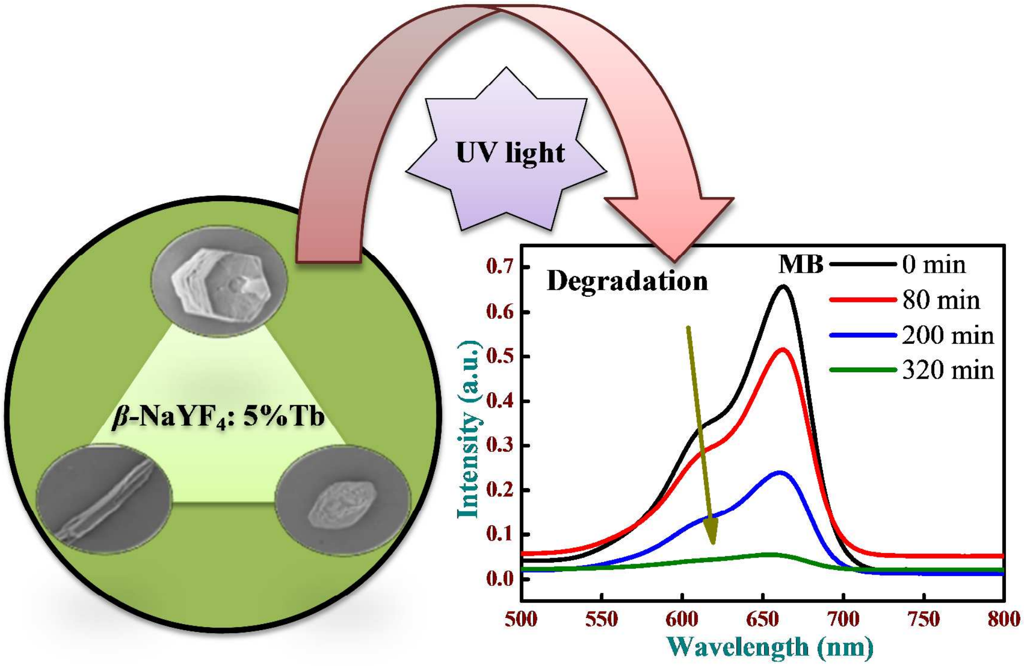

References:

1. Y. Liu, D. Tu, H. Zhuab and X. Chen, *Chem. Soc. Rev*., 2013, **42**, 6924-6958.
2. J. W. Stouwdam and F. C. J. M. van Veggel, *Nano Lett.,* 2002, **2**, 733-737.
3. G. Wang, Q. Peng, and Y. Li, *Accounts of chemical research*., 2011, **44**, 322-332.
4. C. Li and J. Lin, *J. Mater. Chem*., 2010, **20**, 6831-6847.
5. J. C. G. Bunzli and C. Piguet, *Chem. Soc. Rev*., 2005, **34**, 1048-1077.
6. V. Sudarsan, F. C. J. M. van Veggel, R. A. Herring and M. Raudsepp, *J. Mater. Chem.,* 2005, **15**, 1332-1342.
7. C. Sun, C. Carpenter, G. Pratx, L. Xing, *Nanoscale Res Lett* , 2011, **6**, 24.
8. Y. Wang, Y. Liu, Q. Xiao, H. Zhu, R. Lia and X. Chen, *Nanoscale*, 2011, **3**, 3164-3169.
9. Y. Liu, D. Tu, H. Zhu, E. Maa and X. Chen, *Nanoscale*, 2013, **5**, 1369-1384.
10. C. Bouzigues, T. Gacoin, and A. Alexandrou, *ACS Nano*, 2011, **5**, 8488-8505.
11. H. A. Hoppe, *Angew. Chem. Int. Ed*., 2009, **48**, 3572-3582.
12. L. Wang, P. Li, and Y. Li*, Adv. Mater*., 2007, **19**, 3304-3307.
13. F. Wang and X. Liu, *Chem. Soc. Rev*., 2009, **38**, 976–989.
14. M. Haase and H. Schafer, *Angew. Chem. Int. Ed*., 2011, **50**, 5808-5829.
15. M. Banski , M. Afzaal, A. Podhorodecki , J. Misiewicz , A. L. Abdelhady , P. O'Brien, J Nanopart Res., 2012, **14**, 1228.
16. M. Ding, W. Huang, L.Cao, C. Lu , J. Song, Y.Ni, Z.Xu, *Materials Letters*., 2012, **86**, 58-61.
17. L. Wang and Y. Li, *Chem. Mater*., 2007, **19***,* 727-734.
18. S. Zeng, G. Ren, C. Xu and Q. Yang, *CrystEngComm*., 2011, **13**, 1384-1390.

19. K. W. Kramer, D. Biner, G. Frei, H. U. Gudel, M. P. Hehlen, and S. R. Luthi, *Chem. Mater*., 2004, **16***,* 1244-1251.

20. C. Li, J. Yang, Z. Quan, P. Yang, D. Kong, and J. Lin, *Chem. Mater*., 2007, **19***,* 4933-4942.

21. T. Jiang, W. Song, S. Liu, W. Qin, *Journal of Fluorine Chemistry*., 2012, **140**, 70-75.

22. R. Das and P. Poddar, *J. Phys. Chem. C*., 2014, **118**, 13268-13275.

23. S. Sadhu, A. Jaiswal, S. Adyanthaya and P. Poddar, RSC Adv., 2013, **3**, 1933-1940.

24. C. Li, Z. Quan, J. Yang, P. Yang, and J. Lin, *Inorganic Chemistry*., 2007, **46**, 6329-6337.

25. S. Huang, J. Xu, Z. Zhang, X. Zhang, L. Wang, S. Gai, F. He, N. Niu, M. Zhang and P. Yang, *J. Mater. Chem.*, 2012, **22**, 16136-16144.

26. M. Zhang, H. Fan, B. Xi, X. Wang, C. Dong, and Y. Qian, *J. Phys. Chem. C*., 2007, **111***,* 6652-6657.

27. H. Qiu, G. Chen, L. Sun, S. Hao, G. Han and C. Yang, *J. Mater. Chem.,* 2011, **21**, 17202-17208.

28. J. H. Zeng, J. Su, Z.H. Li, R. X. Yan, and Y. D. Li, *Adv.Mater*., 2005, **17**, 2119-2123.

29. F. Zhang, Y. Wan, T. Yu, F. Zhang, Y. Shi, S. Xie, Y. Li, L. Xu, B. Tu, and D. Zhao, *Angew. Chem. Int. Ed*., 2007, **46**, 7976-7979.

30. D. Ma, D. Yang, J. Jiang, P. Cai and S. Huang, *CrystEngComm*., 2010, **12**, 1650-1658.

31. S. G-Grana, F. Hubert, F. Testard, A. G-Martínez, I. Grillo, L. M. L-Marzan, and O. Spalla, *Langmuir*., 2012, **28**, 1453-1459.

32. J. Xiao and L. Qi, *Nanoscale*., 2011, **3**, 1383-1396.

33. N. Zhao and L. Qi, *Adv. Mater*., 2006, **18**, 359-362.

34. N. Zhao, Y. Wei, N. Sun, Q. Chen, J. Bai, L. Zhou, Y. Qin, M. Li, and L. Qi, *Langmuir.,* 2008, **24***,* 991-998.

35. D-K. Ma, S-M. Huang, Y-Y. Yu, Y-F. Xu, and Y-Q. Dong, *J. Phys. Chem. C*., 2009, **113**, 8136-8142.

36. Y. Zheng, J. Lina and Q. Wang, *Photochem. Photobiol. Sci*., 2012, **11**, 1567-1574.

37. C. Hazra, T. Samanta, A. V. Asaithambi and V.Mahalingam, *Dalton Trans*., 2014, **43**, 6623-6630.

38. C. Li, C. Zhang, Z. Hou, L. Wang, Z. Quan, H. Lian, and J. Lin, *J. Phys. Chem. C*., 2009**, 113***,* 2332-2339.

39. M. Ding, C. Lu, L. Cao, Y. Ni and Z. Xu, *CrystEngComm*., 2013, **15**, 8366-8373.

40. D. Tu, Y. Liu, H. Zhu, R. Li, L. Liu, and X. Chen, *Angew. Chem. Int. Ed.,* 2013, **52**, 1128 -1133.

41. C. J. Johnson, E. Dujardin, S. A. Davis, C. J. Murphy and S. Mann, *J. Mater. Chem*., 2002, **12**, 1765-1770.

42. H. Li, C. Kan, Z. Yi, X.Ding, Y. Cao, and J. Zhu, *Journal of Nanomaterials*., 2010, **2010**, 1-8.

43. M. Grzelczak, J. P-Juste, P. Mulvaney and L. M. L-Marzan, *Chem. Soc. Rev*., 2008, **37**, 1783-1791.

44. M. Han, K. Jiang, J. Zhang, W. Yu, Y. Li, Z. Hu and J. Chu, *J. Mater. Chem*., 2012, **22**, 18463-18470.

45. Simanta Kundu, Arik Kar, Amitava Patra, *Journal of Luminescence*, 2012, **132**, 1400–1406

46. L. Xu, J. Shen, C. Lu, Y. Chen, and W. Hou, *Crystal Growth & Design.,* 2009, **9**, 3129- 3136.

47. Z. Xu, X. Kang, C. Li, Z. Hou, C. Zhang, D. Yang, G. Li, and J. Lin, *Inorg. Chem.*, 2010, **49**, 6706-6715.

48. J. Wu, S. Shi, X. Wang, J. Li, R. Zong and W.Chen, *J. Mater. Chem. C.*, 2014, **2**, 2786-2792

49. Y. Xie and C. Yuan, *Applied Catalysis B: Environmental.*, 2003, **46** .251-259.

50. K. Zhang and W. Oh, *Journal of the Korean Ceramic Society.*, 2009, **46**, 561-567.

51. Z. Liu, D. D. Sun, P. Guo, and J. O. Leckie, *Chem. Eur. J.*, 2007, **13**, 1851-1855.

52. A. S. Bhadwal, R. M. Tripathi, R. Kumar Gupta, N. Kumar, R. P. Singh and A. Shrivastav, *RSC Adv.*, 2014, **4**, 9484-9490.

53. P. Dong, Y. Wang, Huihui Li, Hao Li, X. Ma and L. Han, *J. Mater. Chem. A.*, 2013, **1**, 4651-4656.

54. Y. Li and W. Shen, *Chem. Soc. Rev.,* 2014, **43**, 1543-1574.

55. A. Biswas, R. Das, C. Dey, R. Banerjee, and P. Poddar, *Cryst. Growth Des.*, 2014, **14**, 236−239.

56. T. Zhang, T. Oyama, A. Aoshima, H. Hidaka, J. Zhao, N. Serpone, *J. photoch A.*, 2001, **140**, 163-172.